



# Enhanced Electrochemical Properties of $\gamma$ -MnS@rGO Composite as Anodes for Lithium-Ion Batteries

Wonbin Nam<sup>+</sup><sup>[a]</sup>, Honggyu Seong<sup>+</sup><sup>[a]</sup>, Joon Ha Moon<sup>[a]</sup>, Youngho Jin<sup>[a]</sup>, Geongil Kim<sup>[a]</sup>, Hyerin Yoo<sup>[a]</sup>, Taejung Jung<sup>[a]</sup>, MinHo Yang<sup>[b]</sup>, Se Youn Cho,<sup>\*[c]</sup> and Jaewon Choi<sup>\*[a]</sup>

Manganese sulfide (MnS) is a metal chalcogenide with a high theoretical capacity ( $616 \text{ mAh g}^{-1}$ ) and can be used as an alternative anode material for lithium-ion batteries. Generally, metal chalcogenides have intrinsic limitations, such as low stability resulting from volume expansion and poor electronic conductivity. Herein, the authors propose a synthesis strategy of nano-sized  $\gamma$ -MnS, and one-step composite process by the growth of nanoparticles on the surface of reduced graphene

oxide (rGO). These strategies can effectively prevent particle aggregation and enhance an electrochemical stability. The electrochemical performance of the  $\gamma$ -MnS@rGO composite was evaluated using cyclic voltammetry (CV) and galvanostatic charge and discharge measurements. The results showed that the  $\gamma$ -MnS@rGO composite delivered a high specific capacity ( $624 \text{ mAh g}^{-1}$  at  $0.5 \text{ A g}^{-1}$  after 100 cycles), good cycling stability, and excellent rate capability compared to bare  $\gamma$ -MnS.

## Introduction

Lithium-ion batteries (LIBs) have been extensively used in portable electronic devices, electric vehicles (EVs), and energy storage systems due to their high energy density and long cycle life.<sup>[1–5]</sup> The performance of LIBs is significantly determined by the properties of the electrode materials that store and release lithium ions during charge and discharge cycles. Graphite, as a commercially used anode material, exhibits good stability for LIBs. However, its potential for improving energy density is limited due to its low theoretical capacity ( $372 \text{ mAh g}^{-1}$ ). Therefore, it is necessary to develop new anode materials with a high specific capacity.<sup>[6]</sup> In recent years, metal sulfides have attracted attention as potential anode materials for LIBs due to their high theoretical capacity from intrinsic redox reactions (intercalation, conversion, and alloying) capable of delivering high specific capacity.<sup>[7–11]</sup> Manganese sulfide (MnS), a type of metal sulfide, possesses a high theoretical capacity ( $616 \text{ mAh g}^{-1}$ ), low cost, and environmental friendliness.<sup>[12,13]</sup> However, there are still challenges, including poor electrochemical stability and volume

expansion, that need to be addressed for the practical application of MnS for LIBs.<sup>[13,14]</sup>

Introduction of nano-engineering has improved cycle performances of anode materials in recent decades.<sup>[15]</sup> Nano-structures relieve performance degradation resulted from pulverization and improve the lithium-ion transport pathways and their kinetics. But nanomaterials tend to aggregate each other, forming micro-structures that act as barriers to mass transport.<sup>[16]</sup> Meanwhile, carbonaceous materials like reduced graphene oxide (rGO) have been considered as an ideal candidate for the development of composite electrodes due to their high electrical conductivity, large surface area, and chemical stability.<sup>[17–19]</sup> So, a composite strategy with carbonaceous materials can effectively block nanoparticle aggregation, and structural stability can be provided during the charge and discharge process. Recently, nano metal sulfide-based composites with carbonaceous materials with high cycle performances have been extensively reported. For instance, X. Zhou et al. synthesized  $\alpha$ -MnS homogeneously embedded in axial multi-channel carbon nanofibers (MnS@AM-CNF) using the electro-blown spinning technique.<sup>[20]</sup> MnS@AM-CNF exhibited a capacity of  $772 \text{ mAh g}^{-1}$  at a current density of  $0.5 \text{ A g}^{-1}$  after 100 cycles. Also, D. Hu et al. reported  $\alpha$ -MnS nanoparticles anchored on holey graphene (MnS@hG) through the ex-situ synthesis.<sup>[21]</sup> MnS@hG delivered a capacity of  $883 \text{ mAh g}^{-1}$  at a current density of  $0.1 \text{ A g}^{-1}$  after 150 cycles.

In this study, we used two strategies to develop MnS based composite as an anode material: 1) synthesizing nano-sized materials to increase surface area and reaction sites, 2) composite with rGO to enhance electronic conductivity and restrain the aggregation of nanoparticles. We suggest the synthesis method of not only  $\gamma$ -MnS nanoparticles but also  $\gamma$ -MnS@rGO composite through a facile one-pot colloidal synthesis. Herein, the product can be different depending on rGO powder is added or not in the one-pot process.  $\gamma$ -MnS and  $\gamma$ -MnS@rGO were characterized using various techniques such as X-ray diffraction (XRD), scanning electron microscopy (SEM),

[a] W. Nam,<sup>+</sup> H. Seong,<sup>+</sup> J. H. Moon, Y. Jin, G. Kim, H. Yoo, T. Jung, Prof. J. Choi  
Department of Chemistry and Research Institute of Natural Sciences  
Gyeongsang National University  
Jinju 52828 (South Korea)  
E-mail: cjwt0910@gnu.ac.kr

[b] Prof. M. Yang  
Department of Energy Engineering  
Dankook University  
Cheonan 31116 (South Korea)

[c] Dr. S. Y. Cho  
Institute of Advanced Composite Materials  
Korea Institute of Science and Technology  
Wanju-gu 55324 (South Korea)  
E-mail: seyoucho@kist.re.kr

<sup>†</sup> These authors contributed equally to this work.

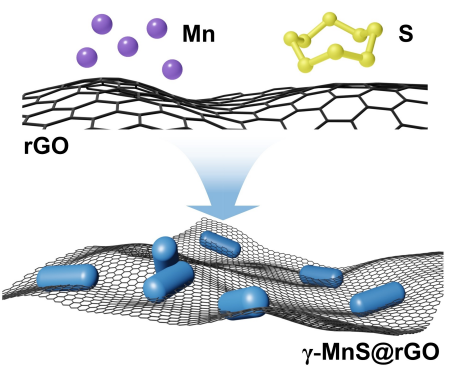
Supporting information for this article is available on the WWW under  
<https://doi.org/10.1002/batt.202300274>

transmission electron microscopy (TEM), X-ray photoelectron spectroscopy (XPS), and electrochemical measurements. In the case of the as-synthesized  $\gamma$ -MnS@rGO, there are  $\gamma$ -MnS nanoparticles homogeneously deposited onto the surface rGO templates, and  $\gamma$ -MnS and rGO interact with each other through C–S–C chemical bond. Moreover, the electrochemical performance of  $\gamma$ -MnS@rGO composite as an anode material for LIBs was investigated, revealing the best cycle performances among reported  $\gamma$ -MnS based anode materials. This study aimed to explore the potential of  $\gamma$ -MnS@rGO composite as a high-performance anode material for LIBs and providing insights into the design and optimization of metal chalcogenide-based electrode materials.

## Results and Discussion

### Morphology and structural characterization

$\gamma$ -MnS and  $\gamma$ -MnS@rGO were prepared by a wet chemical method under the control of parameters including temperature, time, and molar ratio of the reagents (Mn:S).  $\text{MnCl}_2$  was used as Mn source, sulfur as the S source, and commercial rGO as the carbon source. Scheme 1 shows briefly synthetic strategy of  $\gamma$ -MnS@rGO. During all reactants react in a one-pot without an additional process,  $\gamma$ -MnS nanoparticles was uniformly grown on the surface of rGO. The morphology and structure of the as-synthesized  $\gamma$ -MnS and  $\gamma$ -MnS@rGO were analyzed by SEM and TEM.  $\gamma$ -MnS and  $\gamma$ -MnS@rGO nanoparticles had nanorod structures with a diameter of around 40 nm, as shown in SEM images (Figure 1a, d). The TEM image of  $\gamma$ -MnS (Figure 1b) showed that  $\gamma$ -MnS nanoparticles aggregate each other, whereas the TEM image of  $\gamma$ -MnS@rGO (Figure 1e) confirmed that  $\gamma$ -MnS was homogeneously embedded onto rGO with the same particle morphology and size as bare  $\gamma$ -MnS. Through the introduction of rGO matrix, the aggregation of  $\gamma$ -MnS nanoparticles could be inhibited and promoted to react with lithium ion. The HR-TEM images showed a lattice fringe of 0.32 nm, corresponding to the (002) plane of wurtzite  $\gamma$ -MnS (JCPDS No. 40-1289) in Figure 1(c, f). In energy dispersive spectroscopy (EDS) graphs, the atomic compositions of  $\gamma$ -MnS included S at 49.01% and Mn at 50.99% (Figure S1 and Table S1). And the atomic percentages of S and Mn in  $\gamma$ -MnS@rGO were 48.99% and 51.01%, respectively (Figure S2 and Table S2). The results indicated that the ratio of Mn to S was 1:1, and  $\gamma$ -MnS was successfully synthesized on the surface of rGO.



Scheme 1. Illustration of the synthetic strategy of  $\gamma$ -MnS@rGO.

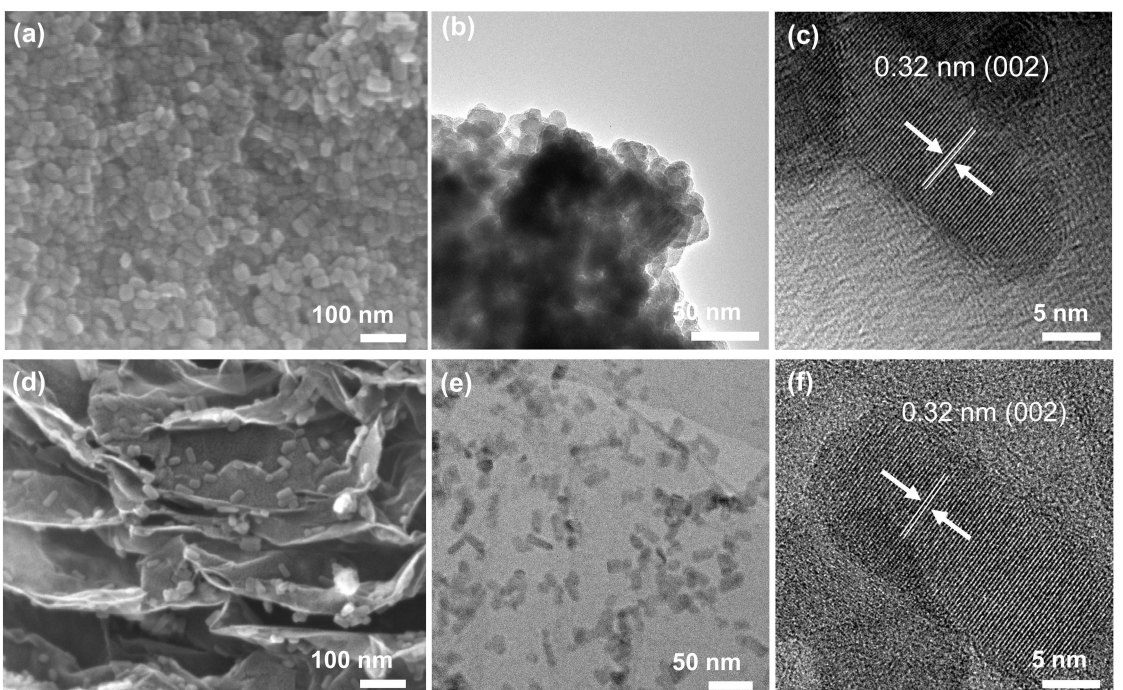


Figure 1. a) SEM image, b) TEM image, and c) HR-TEM image of  $\gamma$ -MnS. d) SEM image, e) TEM image and f) HR-TEM image of  $\gamma$ -MnS@rGO.

The XRD patterns of rGO,  $\gamma$ -MnS, and  $\gamma$ -MnS@rGO are shown in Figure 2(a). Prominent peaks of  $\gamma$ -MnS were detected at  $25.9^\circ$ ,  $27.8^\circ$ ,  $29.4^\circ$ ,  $38.3^\circ$ ,  $45.6^\circ$ ,  $50.1^\circ$ , and  $54.2^\circ$  corresponding to (100), (002), (101), (102), (110), (103), and (112), respectively.<sup>[22]</sup>  $\gamma$ -MnS@rGO had the same peaks as  $\gamma$ -MnS (JCPDS No. 40-1289) and the broad peak at around  $24^\circ$  corresponded to rGO. Thermogravimetric analysis (TGA) was performed to analyze rGO consistency in  $\gamma$ -MnS@rGO. Also, the phase transition of  $\gamma$ -MnS under air was measured, and detailed thermal analysis is provided in the supporting information (Figure S3). In Figure 2(b), the weight increase between 300 to  $400^\circ\text{C}$  indicates the formation of  $\text{MnSO}_4$ . At  $500^\circ\text{C}$ , the combustion of rGO occurred along with the further oxidation of  $\text{MnSO}_4$  and  $\beta$ - $\text{MnSO}_4$  species to  $\text{Mn}_2\text{O}_3$ . After that, the weight loss observed at around  $800^\circ\text{C}$  was attributed to the transformation of  $\text{Mn}_2\text{O}_3$

into  $\text{Mn}_3\text{O}_4$ .<sup>[23,24]</sup> Subsequently, the weight percentage of rGO in  $\gamma$ -MnS@rGO was determined to be 55.3%.

Figure 3(a) shows the Raman spectra of  $\gamma$ -MnS, rGO, and  $\gamma$ -MnS@rGO, confirming their structures. The D band and G band are represented at approximately  $1345\text{ cm}^{-1}$  and  $1586\text{ cm}^{-1}$ , respectively, and the peaks are related to  $\text{sp}^3$  type ( $\text{A}_{1g}$ ) disarranged carbon and  $\text{sp}^2$  type ( $\text{E}_{2g}$ ) graphitized carbon. Also, The Raman graphs of  $\gamma$ -MnS and  $\gamma$ -MnS@rGO have a characteristic peak at  $645\text{ cm}^{-1}$ , indicating the presence of  $\gamma$ -MnS.<sup>[13]</sup> Raman spectra showed that  $\gamma$ -MnS@rGO was successfully synthesized. The surface state and element composition of  $\gamma$ -MnS and  $\gamma$ -MnS@rGO were investigated by XPS analysis. Peaks in Mn 2p spectrum of  $\gamma$ -MnS were assigned to Mn 2p<sub>3/2</sub> ( $640.8\text{ eV}$ ), Mn 2p<sub>1/2</sub> ( $652.2\text{ eV}$ ) (Figure 3b).<sup>[25,26]</sup> The S 2p spectrum of  $\gamma$ -MnS included S 2p<sub>3/2</sub> ( $160.8\text{ eV}$ ), S 2p<sub>1/2</sub> ( $161.9\text{ eV}$ ). And the peak of  $167.5\text{ eV}$  indicates oxidized sulfur ( $\text{SO}_x$ ) due to

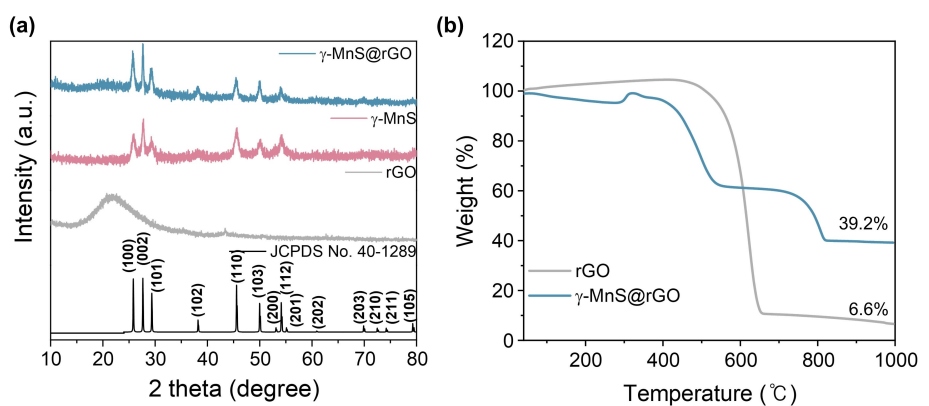


Figure 2. a) XRD patterns of rGO,  $\gamma$ -MnS, and  $\gamma$ -MnS@rGO. b) TGA curve of  $\gamma$ -MnS@rGO, and rGO from room temperature to  $1000^\circ\text{C}$

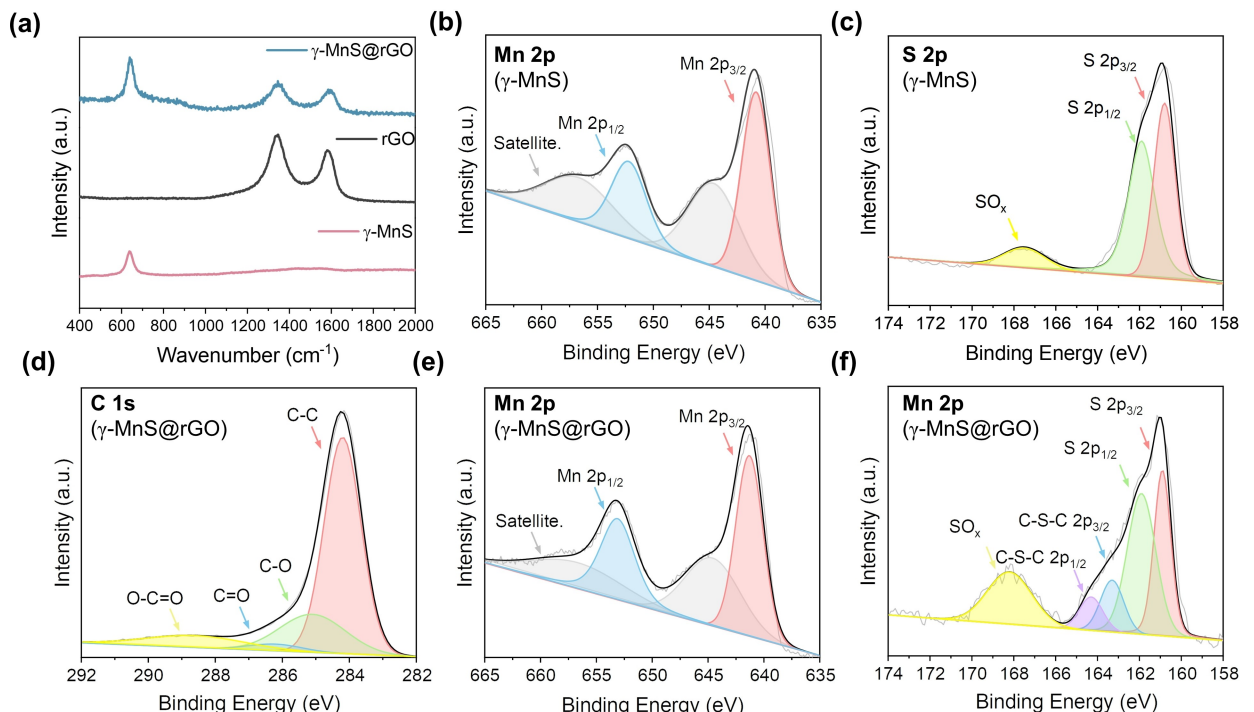


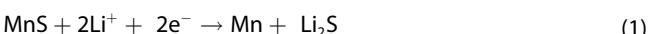
Figure 3. a) Raman spectra of  $\gamma$ -MnS, rGO, and  $\gamma$ -MnS@rGO. XPS spectra of  $\gamma$ -MnS: b) Mn 2p, c) S 2p and  $\gamma$ -MnS@rGO: d) C 1s, e) Mn 2p and f) S 2p.

the exposure of the sample to air (Figure 3c). The Mn 2p spectrum of  $\gamma$ -MnS@rGO showed Mn 2p<sub>3/2</sub> (641.3 eV), and Mn 2p<sub>1/2</sub> (653.1 eV) (Figure 3e). The S 2p spectrum of  $\gamma$ -MnS@rGO exhibited S 2p<sub>3/2</sub> (160.9 eV), S 2p<sub>1/2</sub> (161.9 eV), C–S–C 2p<sub>3/2</sub> (163.3 eV), C–S–C 2p<sub>1/2</sub> (164.3 eV), and SO<sub>x</sub> (168.2 eV) (Figure 3f). The C 1s spectrum of  $\gamma$ -MnS@rGO included four peaks: C=C/C=C (284.2 eV), C–O (285.1 eV), C=O (286.2 eV), and O–C=O (288.6 eV) (Figure 3d).<sup>[27]</sup> Through the emerging of C–S–C peaks in S 2p spectrum of  $\gamma$ -MnS@rGO, a chemical bond between rGO and  $\gamma$ -MnS was verified.

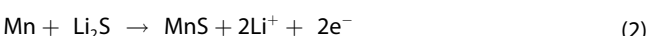
### Electrochemical performance

The electrochemical properties of  $\gamma$ -MnS and  $\gamma$ -MnS@rGO as anode materials for LIBs were analyzed by cyclic voltammetry (CV) curves and galvanostatic charge and discharge profiles (Figure 4). CV analysis of  $\gamma$ -MnS@rGO was conducted over a potential range of 0.01 V to 3.0 V at a scan rate of 0.1 mVs<sup>-1</sup> (Figure 4a). In the first cycle, the two reduction peaks at 0.57 V and 0.11 V were attributed to the formation of a solid electrolyte interface (SEI) layer and the conversion of Mn<sup>2+</sup> to Mn [Equation (1)], respectively. The reduction peak at 0.24 V in the subsequent cathodic scan remained reversible as a conversion process. The peak at 1.27 V in the anodic process indicated that Mn was oxidized to Mn<sup>2+</sup> by the reverse-conversion process [Equation (2)]. Meanwhile, a cathodic peak at 1.57 V and two anodic peaks at 1.92 V and 2.42 V were observed. These irreversible electrochemical reactions are resulted of the conversion reaction of CuS.<sup>[14,28]</sup> The following equations describe the conversion reaction mechanism for lithium-ion storage of MnS.<sup>[29,30]</sup>

[Conversion process]



[Reverse-Conversion process]



In the case of  $\gamma$ -MnS anode (Figure S4a), electrochemical reactions for the conversion process were observed at potential similar to those of the composite anode. However, its redox activity was irreversible and rapidly diminished over time. In addition, CV curves of the commercial rGO anode are presented in Figure S4b. Notably, in the comparison of 5<sup>th</sup> curve of each anode (Figure S4c),  $\gamma$ -MnS@rGO anode showed reversible redox peaks with a high current. This indicates that the electrochemical properties of the  $\gamma$ -MnS@rGO anode are enhanced by our proposed composite strategy.

Figure 4(b) shows  $\gamma$ -MnS@rGO's charge and discharge curves at a current density of 0.5 A g<sup>-1</sup>. The initial CD curve displays distinct plateaus at 1.69 V, 0.75 V, and 0.28 V during discharging and 1.23 V, 1.90 V, and 2.35 V during charging. These observed plateaus align approximately with the peaks observed in the CV curve, and subsequent plateaus are also consistent with the CV behavior. At the 1<sup>st</sup>, 2<sup>nd</sup>, 3<sup>rd</sup>, 4<sup>th</sup>, and 5<sup>th</sup> cycle of  $\gamma$ -MnS@rGO anode, each charge capacity is 766, 717, 696, 670, and 635 mAh g<sup>-1</sup>, and discharge capacity is 1871, 1065, 946, 879, and 824 mAh g<sup>-1</sup>, respectively. In particular, the initial coulombic efficiency is a low value of 41%, attributed to the formation of the SEI layer.<sup>[31,32]</sup> Generally, nano-sized materials possess a large specific surface area capable of contact with electrolyte molecules. Therefore, nanomaterials

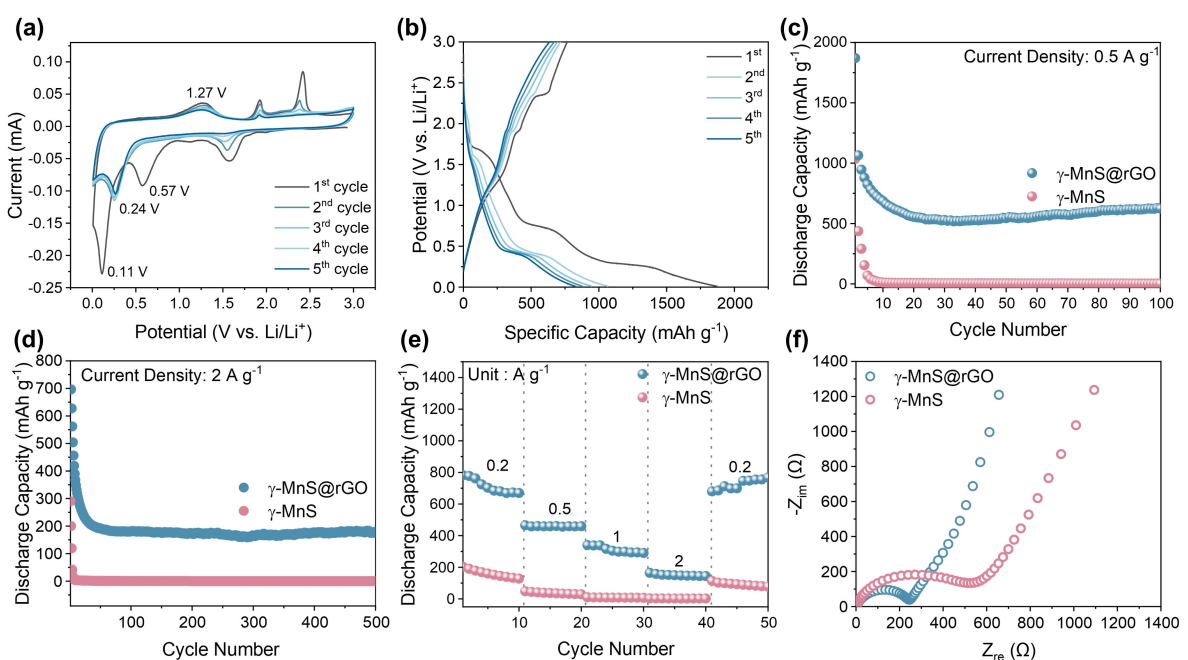


**Figure 4.** a) CV curves of  $\gamma$ -MnS@rGO, b) charge and discharge curves of  $\gamma$ -MnS@rGO at 0.5 A g<sup>-1</sup>, c) Cycling performance of  $\gamma$ -MnS and  $\gamma$ -MnS@rGO at 0.5 A g<sup>-1</sup>, d) High rate performance of  $\gamma$ -MnS@rGO at 2 A g<sup>-1</sup>, e) rate capability of  $\gamma$ -MnS and  $\gamma$ -MnS@rGO of current density range of 0.2 to 2 A g<sup>-1</sup>, f) Nyquist plots of  $\gamma$ -MnS and  $\gamma$ -MnS@rGO.

should intensively undergo the formation of an SEI layer, that is an irreversible lithium storage step in early discharge processes, resulting in the reduction of coulombic efficiency during initial few cycles.

Figure 4(c) illustrates galvanostatic charge and discharge cycling performance at  $0.5 \text{ A g}^{-1}$ . Bare  $\gamma\text{-MnS}$  showed complete degradation of the discharge capacity in the initial few cycles. The  $\gamma\text{-MnS@rGO}$  electrode delivered a discharge capacity of  $624 \text{ mAh g}^{-1}$  after 100 cycles. Also, to optimize the cycle performances of the  $\gamma\text{-MnS@rGO}$  anode, a composite ratio of  $\gamma\text{-MnS:rGO}$  was controlled by adding a different weight of rGO powder (Figure S5). Figure 4(d) shows the cycling performances at a high rate of  $2 \text{ A g}^{-1}$  for 500 cycles.  $\gamma\text{-MnS@rGO}$  exhibited a discharge capacity of  $180 \text{ mAh g}^{-1}$  over 500 cycles. As shown in Figure 4(e), the rate performance of  $\gamma\text{-MnS@rGO}$  exhibited average discharge capacities of 713, 460, 312, and  $151 \text{ mAh g}^{-1}$  at 0.2, 0.5, 1 and  $2 \text{ A g}^{-1}$ , respectively. Then it recovered from  $713 \text{ mAh g}^{-1}$  to  $725 \text{ mAh g}^{-1}$  when the current density returned to  $0.2 \text{ A g}^{-1}$ . Furthermore, when comparing  $\gamma\text{-MnS@rGO}$  with previously reported MnS-based anode materials, the  $\gamma\text{-MnS@rGO}$  in this work delivered the highest discharge capacity among the reported  $\gamma\text{-MnS}$  materials, although it was relatively lower than that of reported  $\alpha\text{-MnS}$  series (Table S3).

Both  $\gamma\text{-MnS}$  and  $\gamma\text{-MnS@rGO}$  anode showed a drastic drop of discharge capacity during the early cycles. It is assumed that the pulverizations of  $\gamma\text{-MnS}$  nanoparticles. Indeed, in a type of  $\gamma\text{-MnS}$  anode, the nanoparticles aggregated after only the first cycle, which it is attributed to a reverse-conversion reaction resulting in the irregular formation of the micro-structure of pulverized MnS nanoparticles (Figure S6). On the other hand,  $\gamma\text{-MnS}$  nanoparticles on rGO matrix endured, and the nanostructured morphology could be observed over not only the first cycle but also 250 cycles at  $2 \text{ A g}^{-1}$  (Figure S6). It was confirmed that the size of nanoparticles decreased as the number of cycles increased, but it was still uniformly distributed on the rGO surface. Furthermore, cycle performances of  $\gamma\text{-MnS@rGO}$  were stabilized after the early cycles' capacity drop was saturated. Meanwhile, in the case of  $\gamma\text{-MnS@rGO}$  anode, discharge capacities exceeding the theoretical capacity of  $\gamma\text{-MnS}$  were observed. It is known that nanomaterials electrodes in the lithium half-cells undergo a reversible formation of a polymer/gel-like SEI layer, showing the pseudo-capacitive lithium storage process.<sup>[33–35]</sup> Based on the CV curve and the charge-discharge profile of  $\gamma\text{-MnS@rGO}$  anode, pseudo-capacitive behaviors can be observed in the low-voltage region (below 0.4 V).

The  $\gamma\text{-MnS@rGO}$  electrode showed stable cycling performance and enhanced discharge capacity and rate performance compared to bare  $\gamma\text{-MnS}$  and the rGO electrode. In order to analyze rGO's contribution of lithium storage in  $\gamma\text{-MnS@rGO}$  electrode, we conducted charge and discharge capacity of rGO at  $0.5 \text{ A g}^{-1}$  (Figure S5f). The rGO electrode showed a discharge capacity of  $200 \text{ mAh g}^{-1}$  after 100 cycles. Because the proportion of rGO in  $\gamma\text{-MnS@rGO}$  is 55.3 wt% in TGA curve (Figure 2b), the calculated capacity contribution of rGO was 17.7%. These electrochemical enhancements of the  $\gamma\text{-MnS@rGO}$  electrode with 82.3% of capacity contribution were attributed to its

composite structure, restraining the aggregation of  $\gamma\text{-MnS}$  anchored on the rGO matrix, in which rGO acted as a structural support for active materials ( $\gamma\text{-MnS}$  nano particles) during the redox process with lithium-ion. The Nyquist plots of  $\gamma\text{-MnS}$  and  $\gamma\text{-MnS@rGO}$  are displayed (Figure 4f). The semicircles in the high-frequency region represent charge transfer resistance ( $R_{ct}$ ) at the electrode and electrolyte interface, while the sloped line in the low frequency region indicates Warburg impedance ( $Z_w$ ). The  $R_{ct}$  value of  $\gamma\text{-MnS@rGO}$  ( $245 \Omega$ ) was lower than  $\gamma\text{-MnS}$  ( $527 \Omega$ ). The results showed that rGO composite improved electronic conductivity of  $\gamma\text{-MnS@rGO}$ .

CV analysis was conducted at scan rates of 0.1, 0.2, 0.5, and  $1 \text{ mV s}^{-1}$  to estimate the kinetics of the  $\gamma\text{-MnS@rGO}$  electrode (Figure 5a). The current increased with increasing scan rate, and the redox peaks shifted due to polarization.<sup>[36]</sup> The equation for the relationship between the current ( $i$ ) and the scan rate ( $v$ ) was:

$$i = av^b \quad (3)$$

$$\log(i) = \log(a) + b \log(v) \quad (4)$$

The value of  $b$  is an important tool of distinction between a diffusion controlled and a capacitive process. A  $b$  value of close to 0.5 indicates a diffusion-controlled process, whereas a value of around 1 indicates a capacitive process.<sup>[37]</sup> As shown in the Figure 5(b), the calculated  $b$  value for the anodic and cathodic peaks of the  $\gamma\text{-MnS@rGO}$  electrode were 0.91 and 0.88, respectively, indicating capacitive behavior. Moreover, to analyze the capacitive contribution to the total current, capacitive current and diffusion-controlled current were quantitatively calculated according to Equation (5).

$$I = k_1 v + k_2 v^{1/2} \quad (5)$$

The terms  $I$ ,  $k_1 v$ , and  $k_2 v^{1/2}$  correspond to the total current, capacitive contribution, and diffusion-controlled contribution, respectively.<sup>[38]</sup> The capacitive contribution of  $\gamma\text{-MnS@rGO}$  was 88% at a scan rate of  $1 \text{ mV s}^{-1}$  (Figure 5c, blue region). As shown in Figure 5(d), the contribution ratios of capacitive current were 57%, 70%, 75% and 88% at scan rates of 0.1, 0.2, 0.5, and  $1 \text{ mV s}^{-1}$ , respectively. These capacitive electrochemical properties of the  $\gamma\text{-MnS@rGO}$  electrode indicate that it had an effectively improved ion diffusion pathway, resulting in accelerated kinetic ion transport for the lithium-ion storage process.

## Conclusions

In summary, a uniform  $\gamma\text{-MnS@rGO}$  composite material was synthesized through facile one-step route by simply adding all precursors together. The characterization of the as-synthesized  $\gamma\text{-MnS@rGO}$  and  $\gamma\text{-MnS}$  nanoparticles showed that they were homogeneously dispersed on the rGO surface and anchored by chemical interactions. Also, electrochemical analysis and galvanostatic charge and discharge battery tests were conducted on a  $\gamma\text{-MnS@rGO}$  electrode fabricated as a coin-type cell (CR2032).

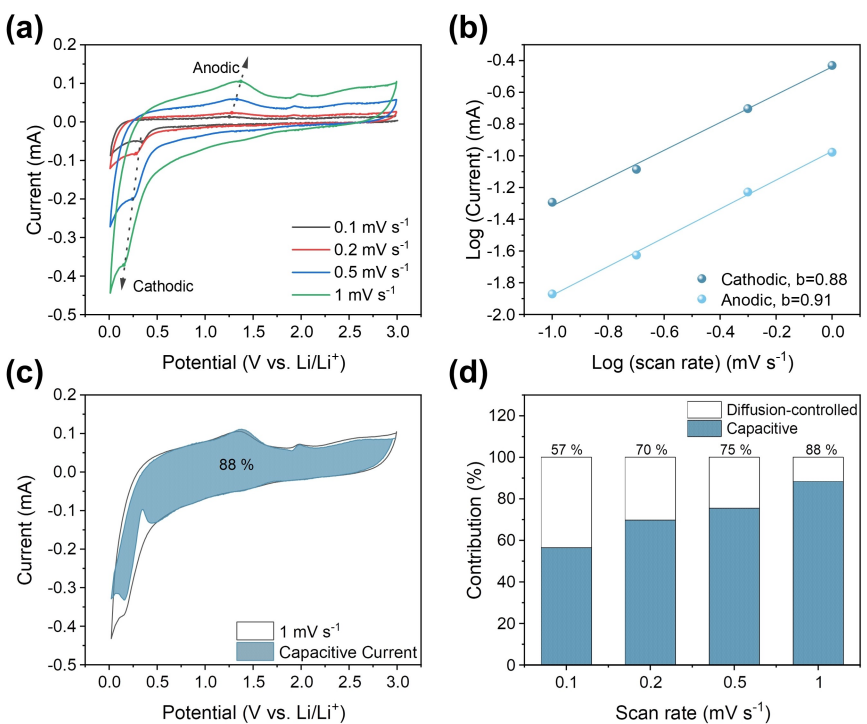


**Figure 5.** a) CV curves of the  $\gamma$ -MnS@rGO electrode at different scan rates. b) The relationship between peak current and scan rate. c) CV curves of the  $\gamma$ -MnS@rGO electrode at 1  $\text{mV s}^{-1}$  with calculated capacitive contribution in the blue region. d) The contribution ratio of capacitive and diffusion-controlled capacities of  $\gamma$ -MnS@rGO at different scan rates.

Cyclic voltammetry revealed the redox activity with lithium-ion and surface capacitive behaviors. Furthermore, the  $\gamma$ -MnS@rGO composite material exhibited excellent discharge capacity (624  $\text{mAh g}^{-1}$  at 0.5  $\text{A g}^{-1}$  after 100 cycles). These outstanding cycle performances of  $\gamma$ -MnS@rGO were attributed to the composite structures, which prevented the aggregation of  $\gamma$ -MnS nanoparticles by anchoring on the rGO surface through chemical binding. The one-pot synthesis strategy in this work brings the improvement of lithium-ion diffusion kinetics and enhanced electrochemical performance. Therefore,  $\gamma$ -MnS@rGO composite is expected to be a promising next-generation anode material for LIBs.

## Experimental Section

### $\gamma$ -MnS@rGO synthesis

Reduced graphene oxide (rGO) powder (25 mg, GRAPHENEALL) was dispersed in oleylamine (7.5 mL, technical grade, 70%, Sigma Aldrich) and the suspension was poured into a 50 mL two-neck Schlenk flask. The mixture was heated at 110 °C for 2 h under vacuum conditions to dry the oleylamine surfactants. Then, sulfur (25.5 mg, 0.795 mmol, Sigma Aldrich) and MnCl<sub>2</sub> (100 mg, 0.795 mmol, Sigma Aldrich) were added at a molar ratio of 1:1 to the well-dried suspension and maintained at 250 °C for 2 h with stirring. After cooling to room temperature, the reaction product was washed with ethanol and hexane and collected by centrifugation to remove any residual compound. Finally, the as-collected precipitants were dried under a vacuum at room temperature and yielding a pinkish-grey color powder. To compare their electro-

chemical behavior,  $\gamma$ -MnS was synthesized by the same method as that for  $\gamma$ -MnS@rGO, except that rGO was not added. Finally,  $\gamma$ -MnS was obtained as a pink-colored powder.

Characterization and Electrochemical measurements were included in the Supporting Information.

## Supporting Information

Supporting Information is available from the Wiley Online Library or from the author.

Additional references cited within the Supporting Information.<sup>[28,39–44]</sup>

## Acknowledgements

W. Nam and H. Seong contributed equally to this work. This work was supported by the National Research Foundation of Korea(NRF) grant funded by the Korea government(MSIT). (NRF-2021R1C1C1011436). This research was supported by “Regional Innovation Strategy (RIS)” through the National Research Foundation of Korea(NRF) funded by the Ministry of Education-(MOE)(2021RIS-003) and following are results of a study on the “Leaders in INdustry-university Cooperation 3.0” Project, supported by the Ministry of Education and National Research Foundation of Korea. This work was supported by the Technological Development for Commercialization by using techbridge platform [RS-2022-00141871] funded by the Ministry of SMEs and Startups (MSS, Korea). This paper is dedicated to

the Department of Chemistry, Sungkyunkwan University, on the occasion of the 70th anniversary

### Conflict of Interests

The authors declare no conflict of interest.

### Data Availability Statement

The data that support the findings of this study are available from the corresponding author upon reasonable request.

**Keywords:** anode materials • lithium-ion batteries •  $\gamma$ -MnS • reduced graphene oxide

- [1] J. B. Goodenough, *Energy Storage Mater.* **2015**, *1*, 158–161.
- [2] J. B. Goodenough, Y. Kim, *Chem. Mater.* **2010**, *22*, 587–603.
- [3] T. Kim, W. Song, D. Y. Son, L. K. Ono, Y. Qi, *J. Mater. Chem. A* **2019**, *7*, 2942–2964.
- [4] V. Etacheri, R. Marom, R. Elazari, G. Salitra, D. Aurbach, *Energy Environ. Sci.* **2011**, *4*, 3243–3262.
- [5] L. M. Z. De Juan-Corpuz, M. T. Nguyen, R. D. Corpuz, T. Yonezawa, N. C. Rosero-Navarro, K. Tadanaga, T. Tokunaga, S. Kheawhom, *ACS Appl. Nano Mater.* **2019**, *2*, 4247–4256.
- [6] Q. Zhang, J. Liao, M. Liao, J. Dai, H. Ge, T. Duan, W. Yao, *Appl. Surf. Sci.* **2019**, *473*, 799–806.
- [7] H. Yuan, L. Kong, T. Li, Q. Zhang, *Chin. Chem. Lett.* **2017**, *28*, 2180–2194.
- [8] Y. Tan, M. Liang, P. Lou, Z. Cui, X. Guo, W. Sun, X. Yu, *ACS Appl. Mater. Interfaces* **2016**, *8*, 14488–14493.
- [9] T. Yang, J. Liu, D. Yang, Q. Mao, J. Zhong, Y. Yuan, X. Li, X. Zheng, Z. Ji, H. Liu, G. Wang, R. Zheng, *ACS Appl. Energ. Mater.* **2020**, *3*, 11073–11081.
- [10] J. Zhao, Y. Zhang, Y. Wang, H. Li, Y. Peng, *J. Energy Chem.* **2018**, *27*, 1536–1554.
- [11] R. Bose, J. Kim, T. H. Kim, B. Koh, N. Go, J. Mun, S. C. Yi, *Bull. Korean Chem. Soc.* **2017**, *38*, 1347–1352.
- [12] R. A. Paredes Camacho, A. M. Wu, X. Z. Jin, X. F. Dong, X. N. Li, H. Huang, *J. Power Sources* **2019**, *437*.
- [13] H. Geng, H. Su, C. Lin, Y. Ma, Y. Zhang, D. Chen, H. Tan, X. Rui, Y. Fang, C. C. Li, *ACS Appl. Energ. Mater.* **2018**, *1*, 4867–4873.
- [14] Y. Ma, Y. Ma, G. T. Kim, T. Diemant, R. J. Behm, D. Geiger, U. Kaiser, A. Varzi, S. Passerini, *Adv. Energy Mater.* **2019**, *9*.
- [15] P. U. Nzereogu, A. D. Omah, F. I. Ezema, E. I. Iwuoha, A. C. Nwanya, *Appl. Surf. Sci. Adv.* **2022**, *9*.
- [16] Y. Sun, N. Liu, Y. Cui, *Nat. Energy* **2016**, *1*.
- [17] X. Y. Pei, D. C. Mo, S. S. Lyu, J. H. Zhang, Y. X. Fu, *Appl. Surf. Sci.* **2019**, *465*, 470–477.
- [18] D. Wang, D. Cai, B. Qu, T. Wang, *CrystEngComm* **2016**, *18*, 6200–6204.
- [19] M. Ahamed, M. Javed Akhtar, M. A. Majeed Khan, H. A. Alhadlaq, *Methods* **2022**, *199*, 28–36.
- [20] X. hai Zhou, K. mei Su, W. min Kang, B. wen Cheng, Z. huan Li, *J. Mater. Sci.* **2020**, *55*, 7403–7416.
- [21] D. Hu, C. Zhu, Y. Yao, S. Liu, X. Meng, H. Yuan, Z. Chen, X. Jiang, Y. Li, S. Zhu, *Appl. Surf. Sci.* **2021**, *542*.
- [22] D. Xu, R. Jiao, Y. Sun, D. Sun, X. Zhang, S. Zeng, Y. Di, *Nanoscale Res. Lett.* **2016**, *11*.
- [23] S. Muhammad, M. W. Nugraha, E. Saputra, N. Arahman, *Water (Switzerland)* **2022**, *14*.
- [24] G. Jian, Y. Xu, L. C. Lai, C. Wang, M. R. Zachariah, *J. Mater. Chem. A* **2014**, *2*, 4627–4632.
- [25] Y. Pei, C. Liu, Z. Han, Z. G. Neale, W. Qian, S. Xiong, Z. Jiang, G. Cao, *J. Power Sources* **2019**, *431*, 75–83.
- [26] P. Tiwari, G. Malik, R. Chandra, *J. Appl. Phys.* **2018**, *124*.
- [27] S. Kumar, S. Riyajuddin, M. Afshan, S. T. Aziz, T. Maruyama, K. Ghosh, *J. Phys. Chem. Lett.* **2021**, *12*, 6574–6581.
- [28] Z. Guo, M. Zhang, F. Wu, Z. Su, L. He, P. Zhou, P. Xu, R. Zou, X. Wang, Q. Huang, *Mater. Today Energy* **2021**, *22*.
- [29] Y. Hao, C. Chen, X. Yang, G. Xiao, B. Zou, J. Yang, C. Wang, *J. Power Sources* **2017**, *338*, 9–16.
- [30] X. Jin, L. Sheng, L. Jiang, Z. Xiao, D. Wang, M. Jiang, X. Lin, X. Zhang, X. Duan, J. Shi, *Mater. Today Chem.* **2022**, *24*.
- [31] Y. Wang, S. Luo, M. Chen, L. Wu, *Adv. Funct. Mater.* **2020**, *30*.
- [32] X. Li, X. Sun, X. Hu, F. Fan, S. Cai, C. Zheng, G. D. Stucky, *Nano Energy* **2020**, *77*.
- [33] S. Laruelle, S. Grageon, P. Poizot, M. Dollé, L. Dupont, J.-M. Tarascon, *J. Electrochem. Soc.* **2002**, *149*, A627.
- [34] S. M. Lee, J. K. Lee, Y. C. Kang, *Chem. Asian J.* **2014**, *9*, 590–595.
- [35] D. Wang, J. Yang, X. Li, D. Geng, R. Li, M. Cai, T. K. Sham, X. Sun, *Energy Environ. Sci.* **2013**, *6*, 2900–2906.
- [36] C. Liu, C. Zhang, H. Fu, X. Nan, G. Cao, *Adv. Energy Mater.* **2017**, *7*.
- [37] J. Feng, S. H. Luo, Y. Zhan, S. X. Yan, P. W. Li, L. Zhang, Q. Wang, Y. H. Zhang, X. Liu, *ACS Appl. Mater. Interfaces* **2021**, *13*, 51095–51106.
- [38] J. Liu, Y. Chang, K. Sun, P. Guo, D. Cao, Y. Ma, D. Liu, Q. Liu, Y. Fu, J. Liu, D. He, *ACS Appl. Mater. Interfaces* **2022**, *14*, 11739–11749.
- [39] Y. Ren, J. Wang, X. Huang, J. Ding, *Solid State Ionics* **2015**, *278*, 138–143.
- [40] J. Beltran-Huarac, O. Resto, J. Carpena-Nuñez, W. M. Jadwiszczak, L. F. Fonseca, B. R. Weiner, G. Morell, *ACS Appl. Mater. Interfaces* **2014**, *6*, 1180–1186.
- [41] S. Gao, G. Chen, Y. Dall'Agnese, Y. Wei, Z. Gao, Y. Gao, *Chem. Eur. J.* **2018**, *24*, 13535–13539.
- [42] J. Ning, D. Zhang, H. Song, X. Chen, J. Zhou, *J. Mater. Chem. A* **2016**, *4*, 12098–12105.
- [43] D. Hu, C. Zhu, Y. Yao, S. Liu, X. Meng, H. Yuan, Z. Chen, X. Jiang, Y. Li, S. Zhu, *Appl. Surf. Sci.* **2021**, *542*.
- [44] R. A. Paredes Camacho, A. M. Wu, X. Z. Jin, X. F. Dong, X. N. Li, H. Huang, *J. Power Sources* **2019**, *437*.

Manuscript received: June 29, 2023

Revised manuscript received: August 22, 2023

Accepted manuscript online: August 22, 2023

Version of record online: August 30, 2023